

ARTICLE

Open Access

# Octahedron distortion-triggered dipole–spin interaction in multiferroic magnetoelectric perovskites

Xiangqian Lu<sup>1</sup>, Renjie Hu<sup>1</sup>, Yabin Zhu<sup>2,3</sup>, Kepeng Song<sup>4</sup> and Wei Qin<sup>1</sup> 

## Abstract

The design of perovskite structures with multiferroic magnetoelectric coupling effects opens up new opportunities in fields such as the creation of next-generation spin-dependent multistate information storage technologies. In this work, we prepared a transition metal-implanted perovskite with multiferroic magnetoelectric coupling, in which both magnetoelectric coupling and a blueshift of photoluminescence were observed. The introduction of transition metal-generated polarized spin interacts with the electronic orbit through spin–orbital coupling to lead to a pronounced octahedron distortion, where the temperature dependence of the dielectric constant undergoes a ferroelectric polarization transition. An external magnetic field could enhance the strength of spin polarization to further affect the magnitude of electric polarization. Moreover, applying an electric field tunes the distortion of the octahedron dependence of electric polarization to feed back to the change in spin polarization. Overall, the spin polarization-induced electric polarization in perovskites provides a unique approach to realizing the room-temperature magnetoelectric coupling of multiferroic materials.


## Introduction

The presence of several ferroic parameters in multiferroic materials<sup>1–3</sup> leads to a series of novel physical phenomena and new physical mechanisms<sup>4,5</sup>. The interaction between magnetism and electricity attracted widespread attention after Oersted accidentally discovered that the electric current produces a force acting on a magnetic needle<sup>6</sup>. The magnetoelectric coupling effect refers to the ability of an applied magnetic field to control the electrical polarization of materials or of an applied electric field to control the magnetization of materials<sup>2,7–9</sup>, which effectively promotes the development of spintronics<sup>10–12</sup>, multistate information storage devices<sup>13,14</sup>, sensing<sup>15,16</sup>, and other fields<sup>17</sup>.

The discovery of multiferroic BiFeO<sub>3</sub> has led to extensive research on the design of multiferroics and magnetoelectric couplings<sup>18,19</sup>. Recently, some inorganic perovskite oxide materials and organic–inorganic hybrid molecular materials have exhibited magnetoelectric coupling effects<sup>18,20–27</sup>. Moreover, many multiferroic structures have been designed to improve performance in the coefficient of magnetoelectric coupling. Ferroelectric/magnetic double perovskite heterojunctions, such as BiFeO<sub>3</sub>/PbTiO<sub>3</sub><sup>28,29</sup>, BiFeO<sub>3</sub>–BiMnO<sub>3</sub><sup>30</sup>, and Bi<sub>2</sub>FeCrO<sub>6</sub>/SrTiO<sub>3</sub><sup>31</sup>, have been designed, where room-temperature magnetoelectric coupling is obtained by means of field-driven phase changes and lattice softening<sup>32,33</sup>. By doping Ni into ferroelectric PbZrO<sub>3</sub>, both large electric polarization and ferromagnetism are generated, leading to strong magnetoelectric coupling with a coefficient of 11.7 mV/(cm Oe)<sup>34</sup>, where the local sublattice interactions among the spin moments and the ferroelectric dipole play a key role in the origin of magnetoelectric coupling. Moreover, in addition to the excellent optoelectronic

Correspondence: Yabin Zhu ([zhuyabin@impcas.ac.cn](mailto:zhuyabin@impcas.ac.cn)) or Kepeng Song ([kpsong@sdu.edu.cn](mailto:kpsong@sdu.edu.cn)) or Wei Qin ([wqin@sdu.edu.cn](mailto:wqin@sdu.edu.cn))  
<sup>1</sup>School of Physics, State Key Laboratory of Crystal Materials, Shandong University, 250100 Jinan, China  
<sup>2</sup>Institute of Modern Physics, Chinese Academy of Sciences, 730000 Lanzhou, China  
Full list of author information is available at the end of the article

© The Author(s) 2023

 **Open Access** This article is licensed under a Creative Commons Attribution 4.0 International License, which permits use, sharing, adaptation, distribution and reproduction in any medium or format, as long as you give appropriate credit to the original author(s) and the source, provide a link to the Creative Commons license, and indicate if changes were made. The images or other third party material in this article are included in the article's Creative Commons license, unless indicated otherwise in a credit line to the material. If material is not included in the article's Creative Commons license and your intended use is not permitted by statutory regulation or exceeds the permitted use, you will need to obtain permission directly from the copyright holder. To view a copy of this license, visit <http://creativecommons.org/licenses/by/4.0/>.

performance of organic–inorganic hybrid perovskites<sup>35–40</sup>, the ferroelectric<sup>41–43</sup> and spin dependence of their properties have attracted interest<sup>37,44–46</sup>. The ferroelectric polarization of organic–inorganic hybrid perovskites contains two parts: the organic dipole moment and the distortion of the octahedron dependence on the dipole moment. Thus, it is expected that if ferromagnetism is involved in organic–inorganic hybrid perovskites, both ferromagnetic and ferroelectric phase-generated spin–dipole interactions will improve the performance of magnetoelectric coupling.

Recently, organic–inorganic hybrid perovskites have been successfully used in the area of photovoltaics due to their fast dissociation and broad absorption<sup>47</sup>. In addition to photovoltaics, perovskites present enormous potential in photodetecting<sup>40</sup> and light-emitting diodes<sup>48</sup>. Moreover, detecting hard X-rays and  $\gamma$ -rays with high energy resolution is critical for medical and industrial applications and homeland security. Organic–inorganic hybrid perovskites have attracted enormous interest for X-ray and  $\gamma$ -ray detection<sup>49,50</sup>. Their valuable role in developing ferroelectricity is still waiting for further exploration<sup>51</sup>. In addition, they contain a chiral cation and exhibit the highest circular dichroism and circularly polarized luminescence intensities<sup>52</sup>. Furthermore, the low leakage current, high mobility, and environmental stability of perovskites have driven the development of next-generation radiation detection and imaging applications<sup>53</sup>.

Herein, we propose a method of transition metal implantation into organic–inorganic hybrid perovskites, which has achieved a pronounced multiferroic magnetoelectric coupling effect at room temperature. The introduction of transition metal-generated spontaneous spin polarization will interact with the electronic orbit through spin–orbital coupling to lead to octahedron distortion, and the temperature dependence of the dielectric constant is studied to confirm the ferroelectricity. Because a magnetic field can decrease the dielectric constant, the recombination rate of electrons and holes increases, resulting in a positive response of photoluminescence to the magnetic field. Furthermore, an external magnetic field could enhance the strength of spin polarization to affect the magnitude of electric polarization, where pronounced magnetoelectric coupling is generated. Moreover, applying an electric field also tunes the distortion of the octahedron dependence of electric polarization to feed back to the change in spin polarization.

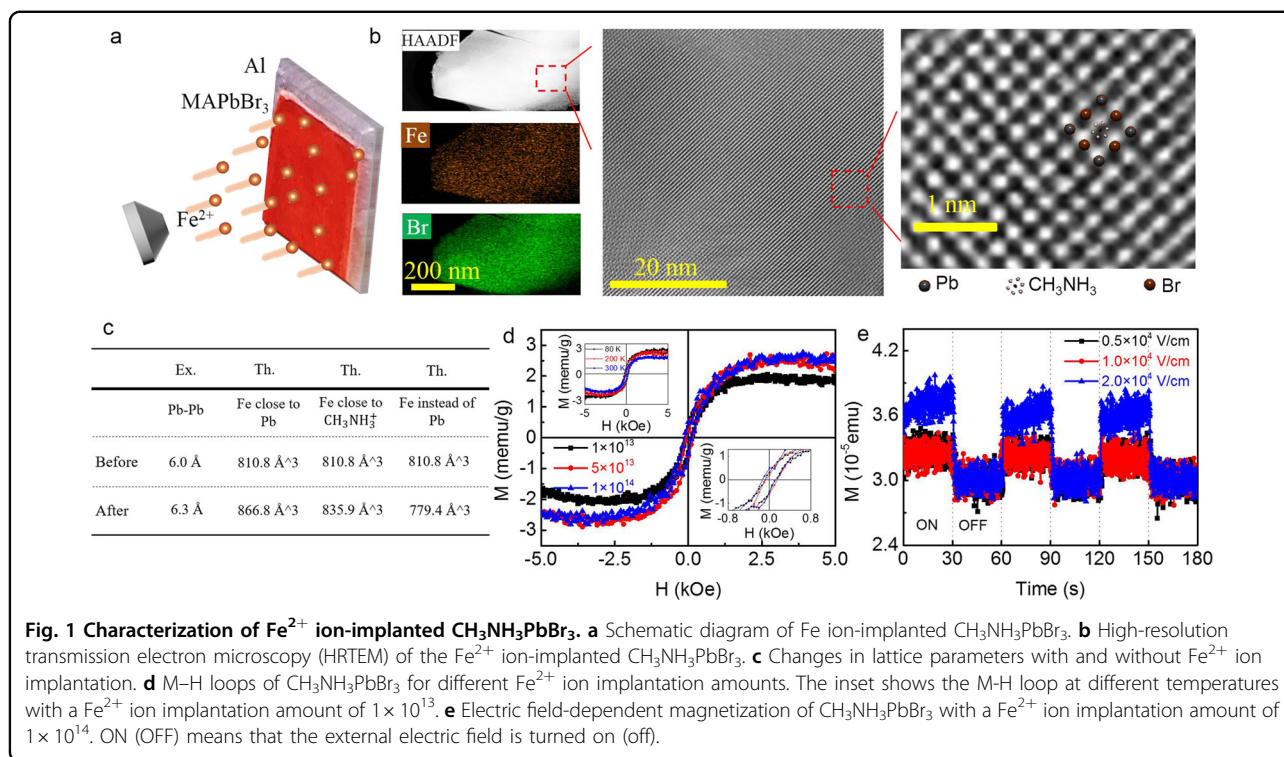
## Results and discussion

$\text{CH}_3\text{NH}_3\text{PbBr}_3$  is an organic–inorganic halide perovskite which can be implanted with the transition metal  $\text{Fe}^{2+}$ . Details of the crystal fabrication and transition metal implantation are presented in the experimental section. Compared with Co and Ni, Fe has a larger

saturation magnetization to enhance the overall strength of spin polarization. Moreover, because the coercivity of Fe is smaller, magnetization can be easily changed by changing the direction of the magnetic field. The architecture of  $\text{Fe}^{2+}$  ion-implanted  $\text{CH}_3\text{NH}_3\text{PbBr}_3$  is presented in Fig. 1a. The elemental analysis of  $\text{Fe}^{2+}$  ion-implanted  $\text{CH}_3\text{NH}_3\text{PbBr}_3$  was studied through high-resolution transmission electron microscopy (HRTEM) and the elemental mappings in Fig. 1b, Supplementary Figs. S1 and S2 show the distributions of Fe, Pb, and Br. As the Fe ion implantation amount increases, the color becomes darker (Supplementary Fig. S3), indicating that implantation affects the electronic structure of perovskites. Moreover, it should be noted that Fe ion implantation will induce larger lattice parameters and unit cell volumes (Fig. 1c and Supplementary Fig. S4). Based on the HRTEM, the distance between neighboring Pb is 6.0 Å for the perovskite without transition metal implantation. Once implantation is finished, the distance increases to 6.3 Å. However, although the site of implanted Fe ions inside perovskites is very difficult to obtain experimentally, theoretical simulation can effectively provide detailed information. The changes in the lattice parameters of Fe ions replacing Pb atoms and interstitial implantation in  $\text{CH}_3\text{NH}_3\text{PbBr}_3$  were simulated using DFT calculations. The former makes the  $\text{CH}_3\text{NH}_3\text{PbBr}_3$  lattice smaller, while the latter makes the lattice larger (Fig. 1c, Supplementary Tables S1–S3). Therefore, the interstitial implantation of Fe ions in perovskites should be the dominant process.

Before Fe ion implantation,  $\text{CH}_3\text{NH}_3\text{PbBr}_3$  does not show spontaneous spin polarization (Supplementary Figs. S5 and S7a). Following the implantation of Fe ions with different ratios, weak ferromagnetism is obtained (Fig. 1d). Moreover, the ferromagnetic properties of  $\text{CH}_3\text{NH}_3\text{PbBr}_3$  with the same number of Fe ions implanted at different temperatures also show a significant difference (inset of Fig. 1d and Supplementary Fig. S6). Importantly, the magnetization of the implanted perovskite can be regulated by an external electric field, showing the magnetoelectric coupling effect at room temperature (Fig. 1e). As described below, the origin of the magnetoelectric coupling in Fe ion-implanted  $\text{CH}_3\text{NH}_3\text{PbBr}_3$  and the mechanism behind the phenomena were studied.

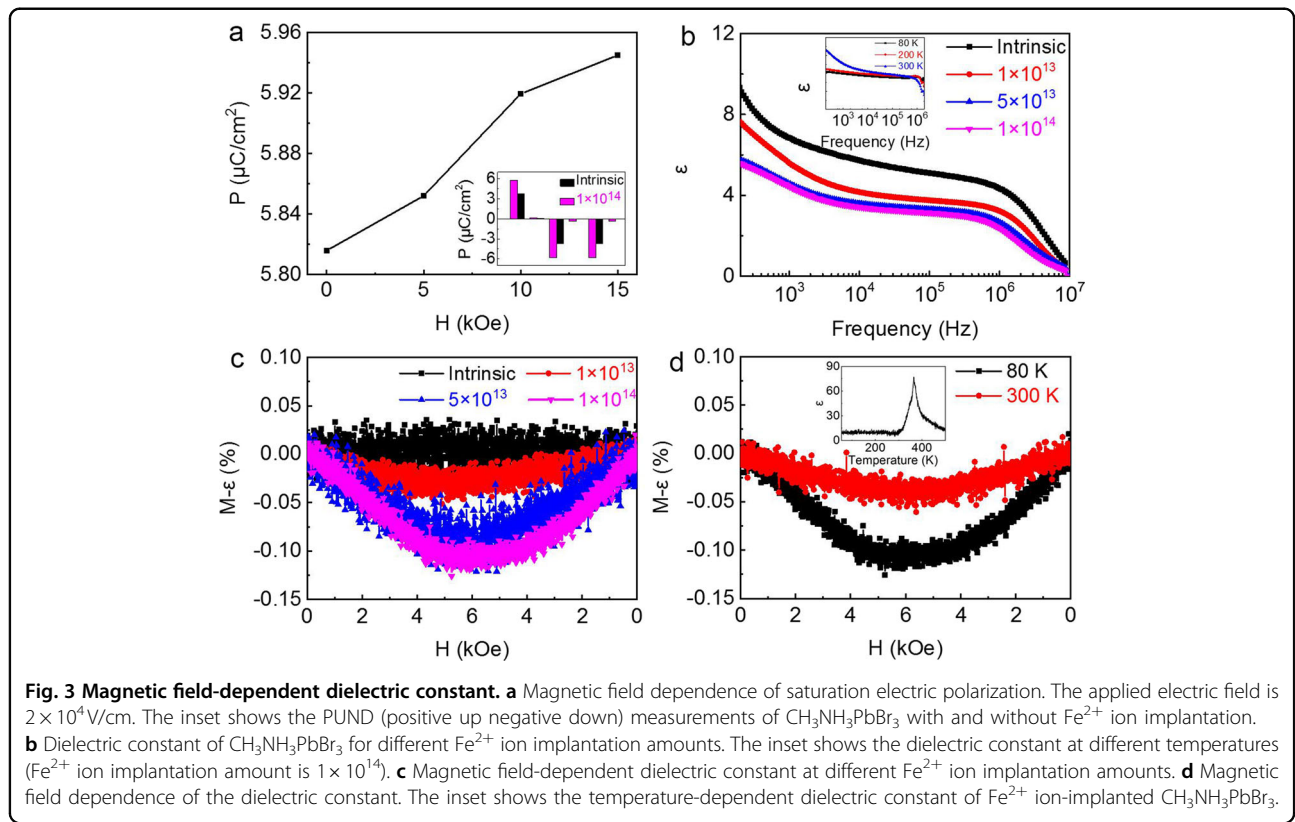
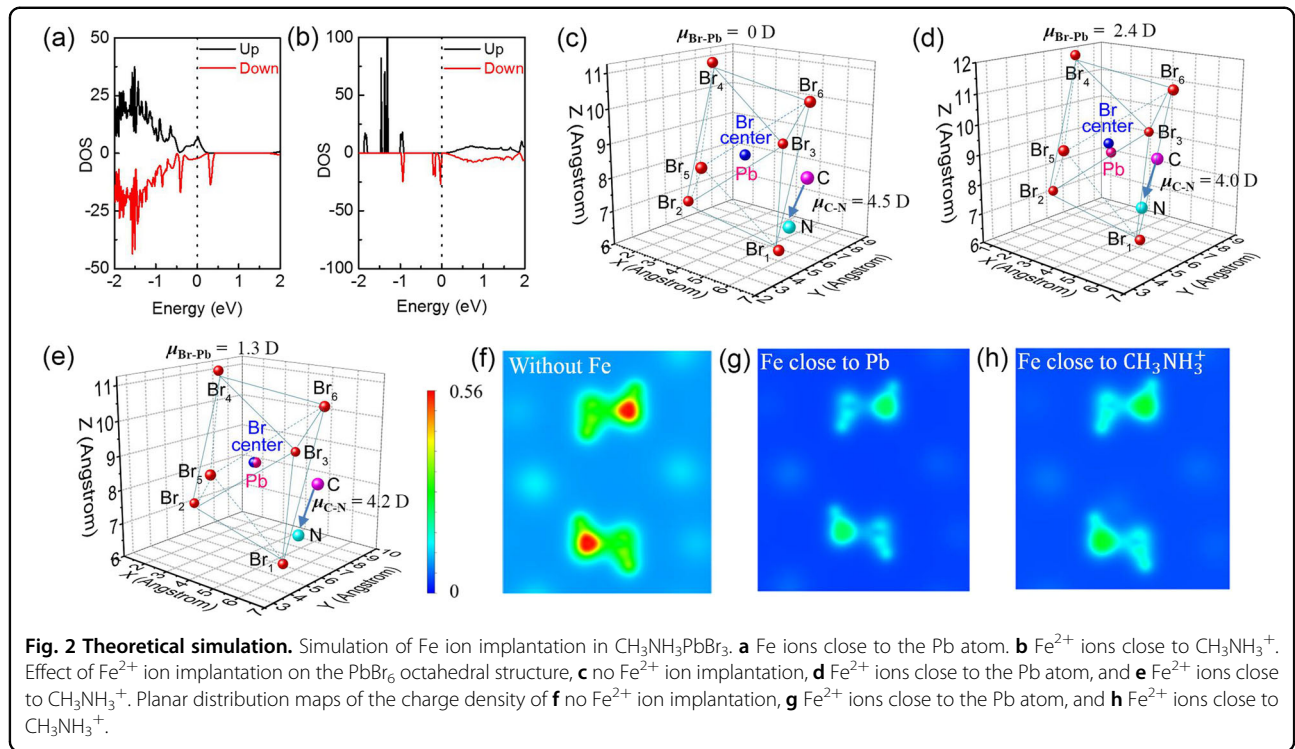
The density of states (DOS) was calculated for the interstitial implantation of Fe ions in perovskites, where asymmetric spin-up and spin-down DOS lead to spin polarization (Fig. 2a, b). Moreover, although the interstitial positions of Fe ions in  $\text{CH}_3\text{NH}_3\text{PbBr}_3$  may be different, the spin-up and spin-down DOSs are always split to generate spontaneous spin polarization (Fig. 2a, b and Supplementary Fig. S7b).  $\text{CH}_3\text{NH}_3\text{PbBr}_3$  without Fe ion implantation possesses a symmetric DOS with a large band gap (Supplementary Fig. S7a). In addition to the



generation of ferromagnetism by implanting Fe ions into perovskites, the distortion of the octahedron and the organic group dependence of the electric dipole moment can also be affected remarkably by spin–orbital coupling (SOC). The implantation of Fe ions generates a polarized spin that will interact with the electronic orbit through SOC to lead to octahedron distortion. The dipole moments of the distorted octahedron were 2.4 D and 1.3 D when the implanted Fe ions were close to Pb and the organic moiety, respectively, as shown in Fig. 2c–e and Supplementary Fig. S8. Before Fe ion implantation, the dipole moment of the perovskite octahedron is zero<sup>54</sup>. However, the dipole moment of the organic part decreases by 0.5 D or 0.3 D with the implantation of Fe ions close to Pb or the organic moiety, respectively. The schematic view of the charge density distribution and charge density differences of organic groups also confirms the effect of Fe ion implantation on the charge distribution of organic groups (Fig. 2f–h; Supplementary Fig. S9). However, it should be noted that Fe ions increase the dipole moment of the octahedron significantly, while the effect on the organic group is much weaker. Thus, based on positive up negative down (PUND) studies, overall electric polarization is enhanced with Fe ion implantation in perovskite, where octahedron distortion could generate spontaneous electric polarization (the inset of Fig. 3a and Supplementary Fig. S10).

The change in electric dipole produced by the implantation of Fe ions will affect the dielectric constant.

As shown in Fig. 3b, with increasing Fe ion implantation, the dielectric constant decreases. Fe ion implantation-induced spin polarization will strongly interact with the octahedron distortion-dependent dipole via SOC, where the dipole bound by spin cannot present a quick response with alternating electric fields. As a result, the dielectric effect becomes weak in Fe ion-implanted perovskites (Fig. 3b). By further increasing the ratio of implanted Fe ions (Fig. 3b) or applying a magnetic field (Fig. 3c) to enhance the increase in spin polarization, the dipole will be further bound. The dielectric effect decreases to induce a negative M–ε (Fig. 3c). In general, magnetization decreases with increasing temperature<sup>55</sup>. As a result, increasing the temperature decreased the spin polarization, leading to a decrease in the dielectric properties (Supplementary Fig. S14). The inset of Fig. 3b shows the C–f curves of CH<sub>3</sub>NH<sub>3</sub>PbBr<sub>3</sub> with Fe ion implantation at different temperatures, and the dielectric constant decreases with decreasing temperature. By increasing the ferromagnetism of the complexes (by increasing the Fe ion ratio or decreasing the temperature), spin polarization will be enhanced to increase the inflorescence on the orbit dependence of dipolar polarization. Thus, as shown in Fig. 3d, with decreasing temperature, a larger spin polarization will strongly interact with dipolar polarization, which provides a channel for the magnetic field to tune the dipolar polarization (Supplementary Fig. S17). Magnetoelectric coupling can be clearly observed in transition metal-implanted perovskites (Fig. 3a). Although



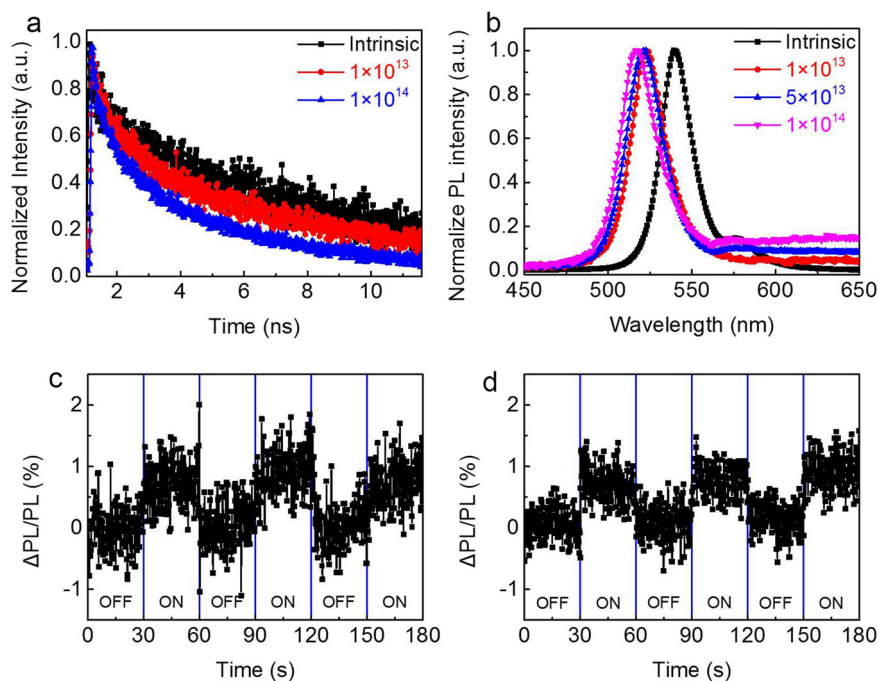


**Fig. 4** Excited state of different  $\text{Fe}^{2+}$  ion implantation amounts and magnetic field-dependent photoluminescence (PL). **a** Fluorescence lifetimes of different amounts of  $\text{Fe}^{2+}$  ions implanted in  $\text{CH}_3\text{NH}_3\text{PbBr}_3$ . The excitation light is linearly polarized. **b** Fluorescence spectra of different amounts of  $\text{Fe}^{2+}$  ions implanted. Magnetic field-dependent PL of different  $\text{Fe}^{2+}$  ion implantation amounts of  $1 \times 10^{13}$  (**c**) and  $1 \times 10^{14}$  (**d**). ON (OFF) means that the magnetic field is turned on (off).

both electric field control of magnetization and magnetic field control of polarization are realized, the magneto-electric transition temperature ranges from 5 K to tens of K<sup>23,24,56,57</sup>, which presents the development of magneto-electric perovskites. The implantation of transition metals into perovskites could increase the transition temperature to room temperature. By analyzing the valence states of Fe in perovskite via X-ray photoelectron spectroscopy (XPS),  $\text{Fe}^{3+}$  and  $\text{Fe}^{2+}$  states coexist (Supplementary Fig. S18). For the ferromagnetic phase transition, magnetization-temperature (M-T) is studied. When the temperature is increased from 10 K to 500 K, the phase transition still cannot be observed. It is expected that although  $\text{Fe}^{2+}$  is implanted, some of the ions may become  $\text{Fe}^{3+}$  and enable ferromagnetic coupling, where the phase temperature is very high (Supplementary Fig. S19). Moreover, with the implantation of Fe ions, the ferroelectric polarization transition temperature is 365 K (inset of Fig. 3d).

Based on the above analysis, the implantation of Fe ions decreases the dielectric constant of  $\text{CH}_3\text{NH}_3\text{PbBr}_3$ . A small dielectric constant will increase the recombination rate<sup>58</sup> to decrease the fluorescence lifetime. As shown in Fig. 4a and Supplementary Fig. S17, increasing the ratio of implanted Fe ions markedly decreases the fluorescence lifetime. Moreover, a smaller dielectric constant could also enlarge the capture distance between the electron and hole, indicating that electrons and holes with larger

distances can easily combine to decrease the fluorescence lifetime. On the other hand, as the distance between the electron and hole increases with the implantation of Fe ions, the energy of emitted photons becomes larger, which causes the PL to blueshift (Fig. 4b). In addition, because a magnetic field can decrease the dielectric constant (Fig. 3c), the recombination rate of electrons and holes increases, resulting in a positive M-PL response (Fig. 4c, d; Supplementary Fig. S21). Furthermore, when the temperature increases, the interaction between the electron and hole becomes weaker, making the band gap of  $\text{CH}_3\text{NH}_3\text{PbBr}_3$  larger, which leads to a blueshift of PL (Supplementary Figs. S23–26).

In contrast, applying an external electric field increases the dipole moment of  $\text{CH}_3\text{NH}_3\text{PbBr}_3$ , which in turn increases the spin polarization through SOC. Therefore, the magnetization of  $\text{CH}_3\text{NH}_3\text{PbBr}_3$  increases when an external electric field is applied (Fig. 5b, c; Supplementary Figs. S24 and 25). For intrinsic  $\text{CH}_3\text{NH}_3\text{PbBr}_3$ , because there is no  $\text{Fe}^{2+}$  implantation, the whole system has no spin polarization. Therefore, the electric field has no effect on the magnetization (Fig. 5a; Supplementary Figs. S27 and 28). As shown in Fig. 5d, the change in magnetization increases as the applied electric field is increased. Furthermore, the magneto-electric coupling coefficient is defined as  $\alpha = \Delta M / \Delta E$ , where  $\Delta M = M(E) - M(E = 0)$  is the electric field-induced change in magnetization. For intrinsic  $\text{CH}_3\text{NH}_3\text{PbBr}_3$ , the

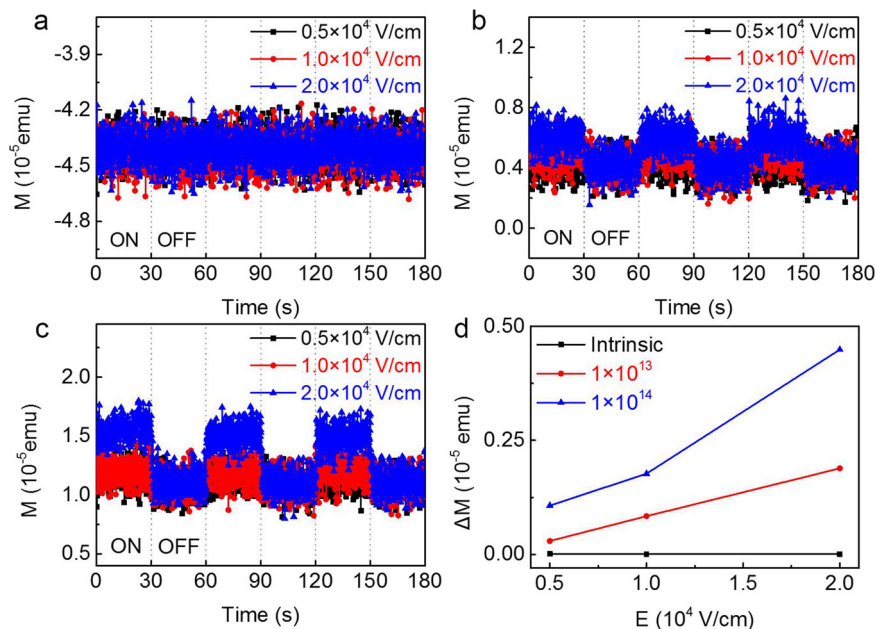


**Fig. 5** Electric field-dependent magnetization with different  $\text{Fe}^{2+}$  ion implantation amounts. **a** Intrinsic, **b**  $1 \times 10^{13}$ , **c**  $1 \times 10^{14}$ . The magnetic field  $H = 1$  kOe. ON and OFF indicate that the external electric field is turned on and off, respectively. **d** Electric field-dependent magnetization change is defined as  $\Delta M = 100 \times M(E) - M(E = 0)$ .

magnetolectric coupling effect is negligible. For  $\text{CH}_3\text{NH}_3\text{PbBr}_3$  with a Fe ion implantation amount of  $1 \times 10^{14}$ , under an external electric field of  $1 \times 10^4$  V/cm, the electric field-induced  $\alpha = 0.18 \times 10^{-9}$  emu cm/V is two times larger than the magnetolectric coupling coefficient ( $0.08 \times 10^{-9}$  emu m/V) with an implantation amount of  $1 \times 10^{13}$ . The magnetolectric coupling effect is enhanced with increasing Fe ion implantation. Overall, transition metal-implanted perovskites are a good platform for potential development in multiferroic magnetolectric devices.

## Conclusion

In summary, we propose a method of Fe ion implantation into organic–inorganic hybrid perovskites to realize multiferroic magnetolectric coupling. Combining theoretical simulation and experimental data shows that the interstitial implantation of metal atoms does not destroy the periodic structure, but the octahedron is distorted. Fe ion implantation not only generates weak ferromagnetism but also predominantly modifies the distortion of the octahedron to enhance electric polarization through spin–orbit coupling. Applying a magnetic field could enhance the strength of spin polarization to further affect the magnitude of electric polarization, where the magnetolectric coupling is induced. Moreover, an electric field could also tune the distortion of the octahedron dependence of electric polarization and, in turn, effect the change in spin polarization. This study provides a new

idea for realizing the room-temperature magnetolectric coupling of multiferroic materials by employing ion implantation and paves the way for a new generation of spin-dependent electronic devices.

## Experimental method

### Preparation of samples

Dimethylformamide (DMF, 99.8%), lead (II) bromide ( $\text{PbBr}_2$ , 99.999%), and methylammonium bromide (MABr, 99.999%) were purchased from Sigma Aldrich. The chemicals were used as received without further purification. The preparation of  $\text{CH}_3\text{NH}_3\text{PbBr}_3$  crystals adopts the controlled antisolvent diffusion method proposed<sup>59</sup>.

### Ion irradiation

Ion irradiation was performed at the 320 kV platform for multidisciplinary research with highly charged ions at the Institute of Modern Physics, Chinese Academy of Sciences, in Lanzhou, China. The as-fabricated samples were irradiated with 3.0 MeV Fe ions to fluences of  $1.0 \times 10^{16}$ ,  $4.0 \times 10^{16}$ , and  $1.0 \times 10^{17}$  ions/cm<sup>2</sup> at room temperature (RT) and  $1.0 \times 10^{17}$  ions/cm<sup>2</sup> at 650 °C, which were denoted as RT-1E16, RT-4E16, RT-1E17, and 650 °C-1E17, respectively. The Stopping and Range of Ions in Matter (SRIM-2013) code with full-cascade simulation mode was used to predict the projected range and irradiation damage profile of the samples. Threshold displacement energies of 0 eV for W atoms and 25 eV for C atoms were adopted.

### Device structure

Cleaned ITO was chosen as the bottom electrode.  $\text{CH}_3\text{NH}_3\text{PbBr}_3$  with/without  $\text{Fe}^{2+}$  ion implantation was dissolved in dimethylformamide (DMF) to a total concentration of 300 mg/ml. Then, the solution was spin-coated on an ITO substrate at 2000 rpm for 120 s and annealed at 80 °C for 20 min. Silver with a thickness of 100 nm was chosen as the top electrode through thermal evaporation.

### Measurements

Transmission electron microscopy (TEM) experiments were performed on a Cs-corrected FEI Titan transmission electron microscope at 300 kV. A direct-detection camera (Gatan K2) was used to acquire high-resolution transmission electron microscopy (HRTEM) images. The dielectric constant measurements were performed with an Agilent E4980A impedance instrument with a frequency range from 20 Hz to 20 MHz. The fluorescence lifetime was measured using an Edinburgh Instruments FLS980 spectrometer with a 400 nm excitation wavelength. The thickness of the material was measured with AFM. The temperature dependence of the M-H loop was measured through a vibrating sample magnetometer (Lakeshore 8604). The photoluminescence was measured with a PG2000 Pro (Idea Optics Co. Ltd.) spectrometer. The polarized state of light is achieved by a polarimeter (PAX1000, Thorlabs) combined with quarter-wave plates and linear polarizers. A magnetic field parallel to the surface of the device is applied by an electromagnet. For the electric field-dependent measurements, a Keithley 2400 (Keithley Instruments Inc., Cleveland, OH, USA) was adopted.

### Calculation details

The ab initio calculations described here were implemented in the Quantum ESPRESSO program with a pseudopotential plane-wave scheme. The projected augmented wave (PAW) method is used to describe the electron–ion interactions. The exchange–correlation interaction is treated by the generalized gradient approximation (GGA) in the form of the Perdew–Burke–Ernzerhof (PBE) functional. The cutoff energy of the plane wave was set to 500 eV. A k-grid of  $5 \times 4 \times 5$  was employed in electronic structure calculations. SOC was incorporated into the electronic structure calculations. The convergence criteria for energy and force were set to  $1 \times 10^{-5}$  eV and 0.01 eV/Å, respectively.

### Acknowledgements

This work was supported by the NSFC (Grant Nos. 91963103 and 62174102), Shandong Province Outstanding Youth Foundation (ZR2020JQ02), Taishan Scholar of Shandong Province (tsqn201812007), and Major Program of Shandong Province Natural Science Foundation (ZR2019ZD43). The authors thank all the staff of the 320 kV platform for multidisciplinary research with

highly charged ions at the Institute of Modern Physics, CAS, for their assistance with Fe ion irradiation.

### Author details

<sup>1</sup>School of Physics, State Key Laboratory of Crystal Materials, Shandong University, 250100 Jinan, China. <sup>2</sup>Institute of Modern Physics, Chinese Academy of Sciences, 730000 Lanzhou, China. <sup>3</sup>School of Nuclear Science and Technology, University of Chinese Academy of Sciences, 100049 Beijing, China. <sup>4</sup>School of Chemistry and Chemical Engineering, Shandong University, 250100 Jinan, China

### Author contributions

W.Q. designed and supervised the project. X.L. designed the experiments and performed the measurements. W.Q., K.S., Y.Z., and Q.L. analyzed the data. M.W. and R.H. provided valuable suggestions. All authors contributed to the discussion and editing of the manuscript.

### Conflict of interest

The authors declare no competing interests.

### Publisher's note

Springer Nature remains neutral with regard to jurisdictional claims in published maps and institutional affiliations.

**Supplementary information** The online version contains supplementary material available at <https://doi.org/10.1038/s41427-023-00485-w>.

Received: 6 August 2022 Revised: 24 April 2023 Accepted: 27 April 2023.  
Published online: 30 June 2023

### References

- Dong, S., Liu, J.-M., Cheong, S.-W. & Ren, Z. Multiferroic materials and magnetoelectric physics: symmetry, entanglement, excitation, and topology. *Adv. Phys.* **64**, 519–626 (2015).
- Eerenstein, W., Mathur, N. D. & Scott, J. F. Multiferroic and magnetoelectric materials. *Nature* **442**, 759–765 (2006).
- Jarillo-Herrero, P., Sapmaz, S., Dekker, C., Kouwenhoven, L. P. & Van Der Zant, H. S. Electron-hole symmetry in a semiconducting carbon nanotube quantum dot. *Nature* **429**, 389–392 (2004).
- Li, M. R. et al. Magnetostriction-polarization coupling in multiferroic  $\text{Mn}_2\text{MnWO}_6$ . *Nat. Commun.* **8**, 2037 (2017).
- Zhai, K. et al. Giant magnetoelectric effects achieved by tuning spin cone symmetry in Y-type hexaferrites. *Nat. Commun.* **8**, 519 (2017).
- Prestes, M. E. D. B. & Silva, C. C. *Teaching Science with Context: Historical, Philosophical, and Sociological Approaches*, 277 (Springer, 2018).
- Li, D. et al. Construction of magnetoelectric composites with a large room-temperature magnetoelectric response through molecular-ionic ferroelectrics. *Adv. Mater.* **30**, 1803716 (2018).
- Ma, J., Hu, J., Li, Z. & Nan, C. W. Recent progress in multiferroic magnetoelectric composites: from bulk to thin films. *Adv. Mater.* **23**, 1062–1087 (2011).
- Spaldin, N. A. & Fiebig, M. The renaissance of magnetoelectric multiferroics. *Science* **309**, 391–392 (2005).
- Fusil, S., Garcia, V., Barthélémy, A. & Bibes, M. Magnetoelectric devices for spintronics. *Annu. Rev. Mater. Res.* **44**, 91–116 (2014).
- Shao, F. et al. Self-assembled hexagonal  $\text{Lu}_{1-x}\text{In}_x\text{FeO}_3$  nanopillars embedded in orthorhombic  $\text{Lu}_{1-x}\text{In}_x\text{FeO}_3$  nanoparticle matrixes as room-temperature multiferroic thin films for memory devices and spintronic applications. *ACS Appl. Nano Mater.* **3**, 7516–7523 (2020).
- Zanolli, Z. Graphene-multiferroic interfaces for spintronics applications. *Sci. Rep.* **6**, 31346 (2016).
- Chanthbouala, A. et al. A ferroelectric memristor. *Nat. Mater.* **11**, 860–864 (2012).
- Zavaliche, F. et al. Electrically assisted magnetic recording in multiferroic nanostructures. *Nano Lett.* **7**, 1586–1590 (2007).
- Sreenivasulu, G., Qu, P., Petrov, V., Qu, H. & Srinivasan, G. Sensitivity enhancement in magnetic sensors based on ferroelectric-bimorphs and multiferroic composites. *Sensors* **16**, 262 (2016).

16. Wang, Y., Li, J. & Viehland, D. Magnetoelectrics for magnetic sensor applications: status, challenges and perspectives. *Mater. Today* **17**, 269–275 (2014).
17. Hill, N. A. Why are there so few magnetic ferroelectrics? *J. Phys. Chem. B* **104**, 6694–6709 (2000).
18. Kimura, T. et al. Magnetic control of ferroelectric polarization. *Nature* **426**, 55–58 (2003).
19. Wang, J. et al. Epitaxial BiFeO<sub>3</sub> multiferroic thin film heterostructures. *Science* **299**, 1719–1722 (2003).
20. Kimura, T., Lawes, G., Goto, T., Tokura, Y. & Ramirez, A. P. Magnetolectric phase diagrams of orthorhombic RMnO<sub>3</sub> (R = Gd, Tb, and Dy). *Phys. Rev. B* **71**, 224425 (2005).
21. Kimura, T., Sekio, Y., Nakamura, H., Siegrist, T. & Ramirez, A. P. Cupric oxide as an induced multiferroic with high-TC. *Nat. Mater.* **7**, 291–294 (2008).
22. Popov, Y. F. et al. Features of the magnetoelectric properties of BiFeO<sub>3</sub> in high magnetic fields. *Low. Temp. Phys.* **27**, 478–479 (2001).
23. Gomez-Aguirre, L. C. et al. Magnetic ordering-induced multiferroic behavior in [CH<sub>3</sub>NH<sub>2</sub>][Co(HCOO)<sub>3</sub>] metal-organic framework. *J. Am. Chem. Soc.* **138**, 1122–1125 (2016).
24. Liu, X. L. et al. Inorganic-organic hybrid molecular materials: from multiferroic to magnetoelectric. *Adv. Mater.* **33**, 2004542 (2021).
25. Stroppa, A., Barone, P., Jain, P., Perez-Mato, J. M. & Picozzi, S. Hybrid improper ferroelectricity in a multiferroic and magnetoelectric metal-organic framework. *Adv. Mater.* **25**, 2284–2290 (2013).
26. Stroppa, A. et al. Electric control of magnetization and interplay between orbital ordering and ferroelectricity in a multiferroic metal-organic framework. *Angew. Chem. Int. Ed. Engl.* **50**, 5847–5850 (2011).
27. Tian, Y. et al. Cross coupling between electric and magnetic orders in a multiferroic metal-organic framework. *Sci. Rep.* **4**, 6062 (2014).
28. Comyn, T. P. et al. Phase-specific magnetic ordering in BiFeO<sub>3</sub>–PbTiO<sub>3</sub>. *Appl. Phys. Lett.* **93**, 232901 (2008).
29. Zhu, W. M., Guo, H. Y. & Ye, Z. G. Structural and magnetic characterization of multiferroic (BiFeO<sub>3</sub>)<sub>1–x</sub>(PbTiO<sub>3</sub>)<sub>x</sub> solid solutions. *Phys. Rev. B* **78**, 014401 (2008).
30. Fernandez-Posada, C. M. et al. A novel perovskite oxide chemically designed to show multiferroic phase boundary with room-temperature magnetoelectricity. *Nat. Commun.* **7**, 12772 (2016).
31. Nechache, R. et al. Epitaxial patterning of Bi<sub>2</sub>FeCrO<sub>6</sub> double perovskite nanostructures: multiferroic at room temperature. *Adv. Mater.* **23**, 1724–1729 (2011).
32. Kitamura, M. et al. Relationship between charge redistribution and ferromagnetism at the heterointerface between the perovskite oxides LaNiO<sub>3</sub> and LaMnO<sub>3</sub>. *Phys. Rev. B* **100**, 245132 (2019).
33. Yáñez-Vilar, S. et al. Multiferroic behavior in the double-perovskite Lu<sub>2</sub>MnCoO<sub>6</sub>. *Phys. Rev. B* **84**, 134427 (2011).
34. Kumari, S. et al. Room-temperature large magnetoelectricity in a transition metal doped ferroelectric perovskite. *Phys. Rev. B* **104**, 174415 (2021).
35. Brenner, T. M., Egger, D. A., Kronik, L., Hodes, G. & Cahen, D. Hybrid organic–inorganic perovskites: low-cost semiconductors with intriguing charge-transport properties. *Nat. Rev. Mater.* **1**, 15007 (2016).
36. Seo, H. K. et al. Efficient flexible organic/inorganic hybrid perovskite light-emitting diodes based on graphene anode. *Adv. Mater.* **29**, 1605587 (2017).
37. Wang, J. et al. Spin-optoelectronic devices based on hybrid organic–inorganic trihalide perovskites. *Nat. Commun.* **10**, 129 (2019).
38. Yang, Z., Rajagopal, A. & Jen, A. K. Ideal bandgap organic–inorganic hybrid perovskite solar cells. *Adv. Mater.* **29**, 1704418 (2017).
39. Zhao, Y. & Zhu, K. Organic–inorganic hybrid lead halide perovskites for optoelectronic and electronic applications. *Chem. Soc. Rev.* **45**, 655–689 (2016).
40. Zhou, J. & Huang, J. Photodetectors based on organic–inorganic hybrid lead halide perovskites. *Adv. Sci.* **5**, 1700256 (2018).
41. Li, L. et al. A potential Sn-based hybrid perovskite ferroelectric semiconductor. *J. Am. Chem. Soc.* **142**, 1159–1163 (2020).
42. Park, I. H. et al. Ferroelectricity and Rashba effect in a two-dimensional Dion-Jacobson hybrid organic–inorganic perovskite. *J. Am. Chem. Soc.* **141**, 15972–15976 (2019).
43. You, Y.-M. et al. An organic–inorganic perovskite ferroelectric with large piezoelectric response. *Science* **357**, 306–309 (2017).
44. Li, M. et al. Magnetodielectric response from spin-orbital interaction occurring at interface of ferromagnetic Co and organometal halide perovskite layers via Rashba effect. *Adv. Mater.* **29**, 1603667 (2017).
45. Wang, J. et al. Tunable spin characteristic properties in spin valve devices based on hybrid organic–inorganic perovskites. *Adv. Mater.* **31**, 1904059 (2019).
46. Wang, M. et al. Optically induced static magnetization in metal halide perovskite for spin-related optoelectronics. *Adv. Sci.* **8**, 2004488 (2021).
47. Hao, F., Stoumpos, C. C., Cao, D. H., Chang, R. P. H. & Kanatzidis, M. G. Lead-free solid-state organic–inorganic halide perovskite solar cells. *Nat. Photonics* **8**, 489–494 (2014).
48. Xiao, Z. et al. Efficient perovskite light-emitting diodes featuring nanometre-sized crystallites. *Nat. Photonics* **11**, 108–115 (2017).
49. Liu, F. et al. Recent progress in halide perovskite radiation detectors for gamma-ray spectroscopy. *ACS Energy Lett.* **7**, 1066–1085 (2022).
50. Wu, H., Ge, Y., Niu, G. & Tang, J. Metal halide perovskites for X-ray detection and imaging. *Matter* **4**, 144–163 (2021).
51. Shi, P. P. et al. Two-dimensional organic–inorganic perovskite ferroelectric semiconductors with fluorinated aromatic spacers. *J. Am. Chem. Soc.* **141**, 18334–18340 (2019).
52. Lin, J. T. et al. Tuning the circular dichroism and circular polarized luminescence intensities of chiral 2D hybrid organic–inorganic perovskites through halogenation of the organic ions. *Angew. Chem. Int. Ed. Engl.* **60**, 21434–21440 (2021).
53. He, X. et al. Recent development of halide perovskite materials and devices for ionizing radiation detection. *Chem. Rev.* **4**, 1207–1261 (2023).
54. Jin, J. et al. A new perspective and design principle for halide perovskites: ionic octahedron network (ION). *Nano Lett.* **21**, 5415–5421 (2021).
55. Mahendiran, R. et al. Ultrasharp magnetization steps in perovskite manganites. *Phys. Rev. Lett.* **89**, 286602 (2002).
56. Taniguchi, K. et al. Magneto-electric directional anisotropy in polar soft ferromagnets of two-dimensional organic–inorganic hybrid perovskites. *Angew. Chem. Int. Ed. Engl.* **60**, 14350–14354 (2021).
57. Tian, Y. et al. High-temperature ferroelectricity and strong magnetoelectric effects in a hybrid organic–inorganic perovskite framework. *Phys. Status Solidi Rapid Res. Lett.* **9**, 62–67 (2015).
58. Hughes, M. P. et al. Charge recombination dynamics in organic photovoltaic systems with enhanced dielectric constant. *Adv. Funct. Mater.* **29**, 1901269 (2019).
59. Zhang, L. et al. Exploring anisotropy on oriented wafers of MAPbBr<sub>3</sub> crystals grown by controlled antisolvent diffusion. *Cryst. Growth Des.* **18**, 6652–6660 (2018).